ADVANCED FUNCTIONAL MATERIALS
www.afm-journal.de

Wide Detection Range Flexible Pressure Sensors Based on 3D Interlocking Structure TPU/ZnO NWs

Jiang He, Siyuan Wang, Renhou Han, Yue Liu, Wenchao Gao, Rongrong Bao,* and Caofeng Pan**

The high sensitivity and wide linear sensing range are two crucial performance parameters for pressure sensors. This paper presents a flexible pressure sensor based on a 3D interlocking structure resembling the biomimetic dog-tail grass. The 3D interlocking structure of TPU/ZnO nanowires (NWs) uniformly increases with the applied pressure, resulting in a proportional increase in the contact area. Simultaneously, ZnO NWs form an upper sparse and lower dense structure on the TPU skeleton, enabling it to withstand exceptionally high pressures. Leveraging these advantages, the flexible pressure sensor exhibits elevated sensitivity (29.7 kPa^{-1}) and an ultra-wide linear sensing range (up to 2250 kPa), representing a significant improvement compared to prior research. The sensor demonstrates outstanding performance in terms of repeatability and stability. Furthermore, applications in wearable electronic devices and pixel analysis in pressure array configurations are demonstrated, showcasing high performance achieved through straightforward and cost-effective fabrication methods, thereby offering a promising strategy for future developments in flexible electronic devices.

1. Introduction

Flexible pressure sensors are electronic devices capable of converting pressure signals into electrical signals. They exhibit tremendous potential in applications such as wearable electronic devices, the Internet of Things, and soft robotics, garnering widespread attention.[1] To perform effectively in these fields, such sensors must achieve both high sensitivity for precise pressure detection and a wide detection range to capture both subtle forces (e.g., touch) and large forces (e.g., hit).[2] In recent years, numerous studies have sought to enhance sensor sensitivity by optimizing sensing mechanisms and device structures.[3] However, these sensors often have limited operating ranges and tend to saturate under high pressures, constraining their applications in intense motion detection and robotic perception under extreme conditions.[4] Existing wide-range pressure sensors, on the other hand, generally exhibit relatively low sensitivity.[5] It is urgently needed to obtain pressure sensors that perform both high sensitivity and wide detection range.

Among all types of sensing mechanisms, resistive-type sensors have gained extensive use due to their high sensitivity, relatively wide operating range, simple structure, and signal stability.[2,6] The sensing principle of most flexible resistive sensors involves inducing changes in resistance by altering the conductive pathway between electrodes. Common research approaches for achieving highly sensitive flexible resistive sensors include reducing the initial contact area of the conductive material and increasing the contact area under compression. Consequently, researchers have proposed various micro/nanostructures such as pyramids, hemispheres, columns, interlocking patterns, and multilayer structures to attain this objective.[7] Compared to devices without structures, these prevalent convex-shaped structures reduce the initial resistance, contributing to enhanced sensor sensitivity. However, these structures tend to saturate after compression, resulting in a limited high-sensitivity sensing range and a decrease in sensitivity with increasing pressure. Another emerging strategy for simultaneously achieving high sensitivity and a broad linear detection range involves the use of a multilayer structure. This design utilizes multiple layers with varying geometric shapes to linearly increase the contact area, distributing the applied stress across each layer to provide an exceptionally wide sensing range while maintaining relatively high sensitivity.[8] Nevertheless, the ability to tune linearity typically necessitates three or more sensitive layers, making the fabrication process complex.

In recent years, the design of a sensitive layer with an interlocking structure has garnered attention from many researchers. This approach has the potential to balance the dual requirements

J. He, S. Wang, R. Han, Y. Liu, W. Gao
Beijing Institute of Nanoenergy and Nanosystems
Chinese Academy of Sciences
Beijing 101400, P. R. China
E-mail: gaowenchao@binn.cas.cn
S. Wang
School of Nanoscience and Technology
University of Chinese Academy of Sciences
Beijing 100049, China
R. Bao, C. Pan
Institute of Atomic Manufacturing
Beihang University
Beijing 100191, P. R. China
E-mail: baorongrong@buaa.edu.cn; pancaofeng@buaa.edu.cn

The ORCID identification number(s) for the author(s) of this article can be found under https://doi.org/10.1002/adfm.202418791

DOI: 10.1002/adfm.202418791

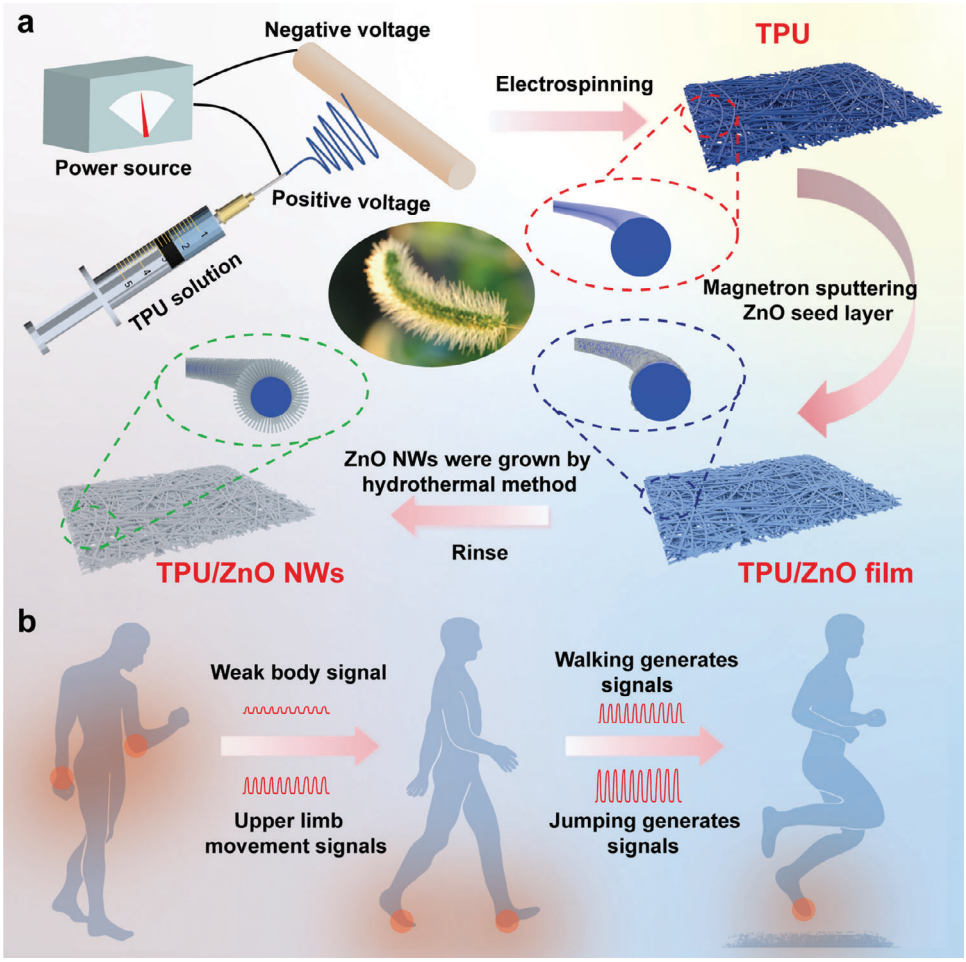

Figure 1. Preparation of the Sensitive Layer and Wide-Range Detection Signal. a) Schematic diagram illustrating the preparation process of TPU/ZnO NWs based on the sensitive layer. b) Wide-range detection of human motion signals.

of high sensitivity and a wide linear detection range to some extent.[9] However, due to the complexity of the fabrication process, achieving large-area and uniformly sized interlocking structures remains challenging.

In this study, we developed a high-performance flexible pressure sensor with a 3D interlocking thermoplastic urethane (TPU)/zinc oxide (ZnO) nanowires (NWs) structure using a simple and efficient fabrication method. The flexible pressure sensor, inspired by a biomimetic 3D interlocking structure resembling dog-tail grass, exhibits excellent sensing capabilities with high sensitivity (29.7 kPa^{-1}) and an ultra-wide sensing detection range (≈2250 kPa). The pressure sensor demonstrates remarkably high stability even under extremely high pressures. Additionally, various performance aspects, including repeatability, low detection limit, dynamic response, and response/recovery time, were systematically evaluated. Thin films of TPU fibers were prepared through electrospinning, and ZnO NWs were grown on the fiber surface using a simple hydrothermal method, forming a multi-layered interlocking structure between the fibers. Experimental results indicate a significant improvement in the sensing performance of the TPU/ZnO NWs structure compared to the TPU/ZnO film structure, underscoring the crucial role of the TPU/ZnO NWs multi-layered 3D interlocking structure in sensitivity and linear sensing range. Furthermore, by monitoring human motion signals, the device demonstrates excellent pressure responsiveness to both subtle body signals and high-pressure motion signals. Lastly, array integration enables the identification of the applied position and pressure level of weights and the analysis of the primary force points when fingers are pressed. This approach represents a straightforward and efficient method for fabricating 3D high-sensitivity and wide linear detection range pressure sensors, holding significant potential for applications in wearable electronic devices, human-machine interfaces, and intelligent robotics.

2. Results and Discussion

To fabricate a flexible pressure sensor with high sensitivity and a wide linear detection range, a biomimetic dog-tail grass structure was proposed using TPU electrospinning as the framework, with tightly wrapped zinc oxide nanowires around the TPU electrospun fibers. As illustrated in **Figure 1a**, TPU filaments were initially collected on a rotating spindle using electrospinning technology. Subsequently, ZnO nanoparticles were deposited onto the

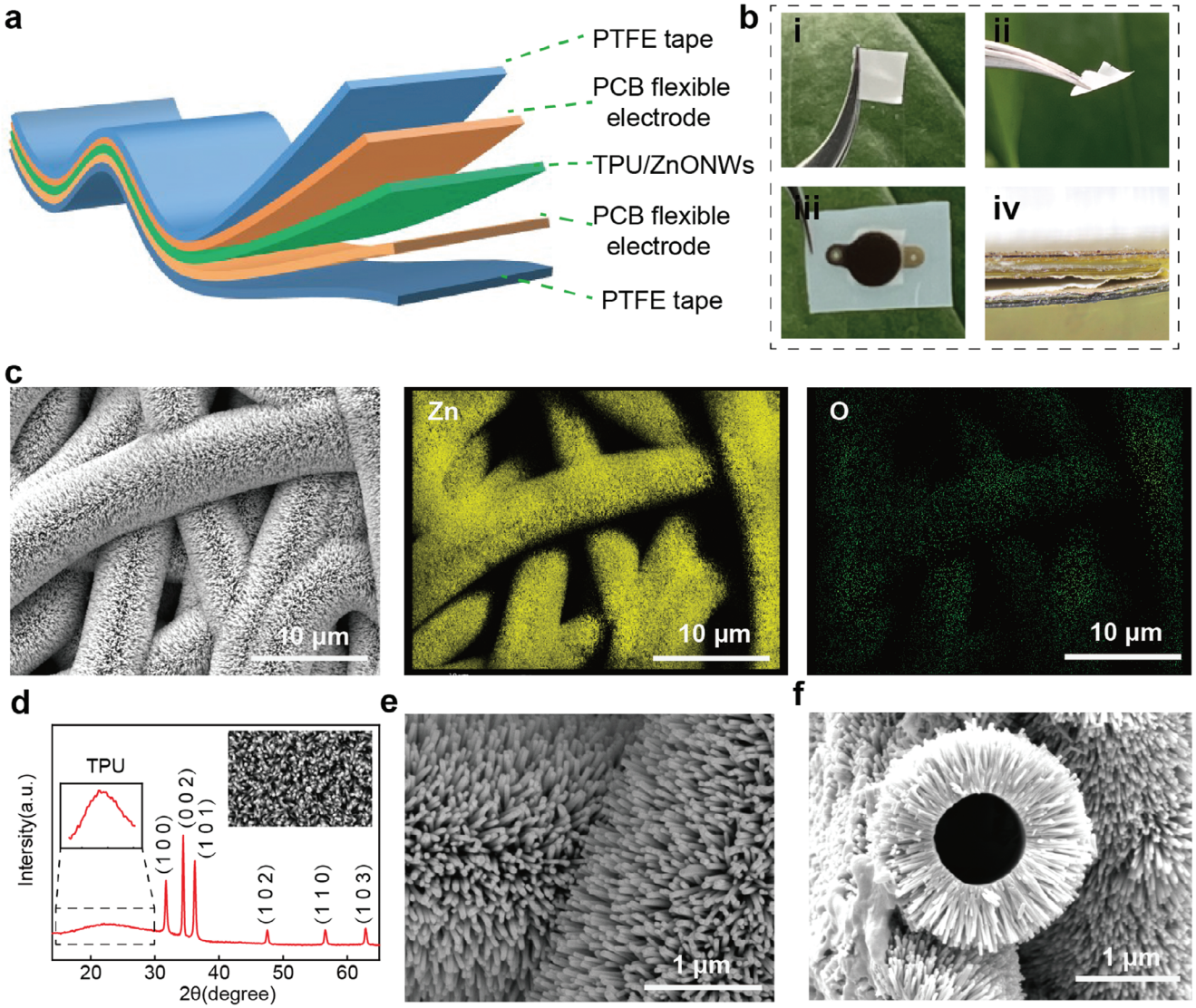

Figure 2. Characterization of Device Structure and Sensitive Layer. a) Schematic diagram of device structure. b) i) Optical Photographs of the Sensitive Layer, ii) Demonstrating the Flexibility of the Sensitive Layer, iii) Optical Photographs of Individual Devices, iv) Cross-Sectional View of the Device. c) Energy Dispersive Spectrometer (EDS) Elemental Mapping Image of TPU/ZnO NWs. d) X-ray Diffraction (XRD) Spectra of TPU/ZnO NWs. e) Magnified Electron Micrograph of Zinc Oxide Nanowires. f) Cross-Sectional Electron Microscopy Images of TPU/ZnO NWs.

rotating TPU scaffold as a seed layer through magnetron sputtering. Finally, zinc oxide nanowires were grown via a hydrothermal process, creating a structure resembling the morphology of dog-tail grass and completing the preparation of the interlocking structure sensor's sensitive layer. Figure 1b demonstrates the capability of the same flexible pressure sensor to perceive both weak pressure signals (such as pulses) and larger pressure signals (such as those from the sole of the foot). This highlights the sensor's extensive detection range and its significant potential in wearable technology applications.

As depicted in **Figure** 2a, the single device subjected to experimentation primarily comprises three components: the sensitive layer TPU/ZnO NWs, two PCB flexible electrodes with one side coating gold, and two layers of PTFE tape as encapsulation layers. Optical photographs of the sensitive layer (Figure 2b-i) and the individual device (Figure 2b-iii) are presented in Figure 2b. Figure 2b-ii illustrates the flexible folding of the TPU/ZnO NWs sensitive layer, indicating its high flexibility. The cross-section diagram of the device (Figure 2b–vi) corresponds to Figure 2a, revealing the five-layer structure of a single device. Refer to Figure S1 (Supporting Information) for a detailed annotation of the cross-section diagram. Figure 2c displays the EDS spectrum of the TPU/ZnO NWs sensitive layer, demonstrating the uniform distribution of zinc and oxygen elements on the TPU framework. Both electron microscopy and EDS images confirm the dense coverage of zinc oxide nanowires on the spinning skeleton. In Figure 2d, at $2\theta = 22.3°$, a lower peak is observed, mainly generated by the spinning skeleton of TPU, aligning with the peak of TPU reported in the literature.[10a] Peaks at 2θ of 31.75°, 34.42°, 36.24°, 47.54°, 56.58°, and 62.86° correspond to the six crystal

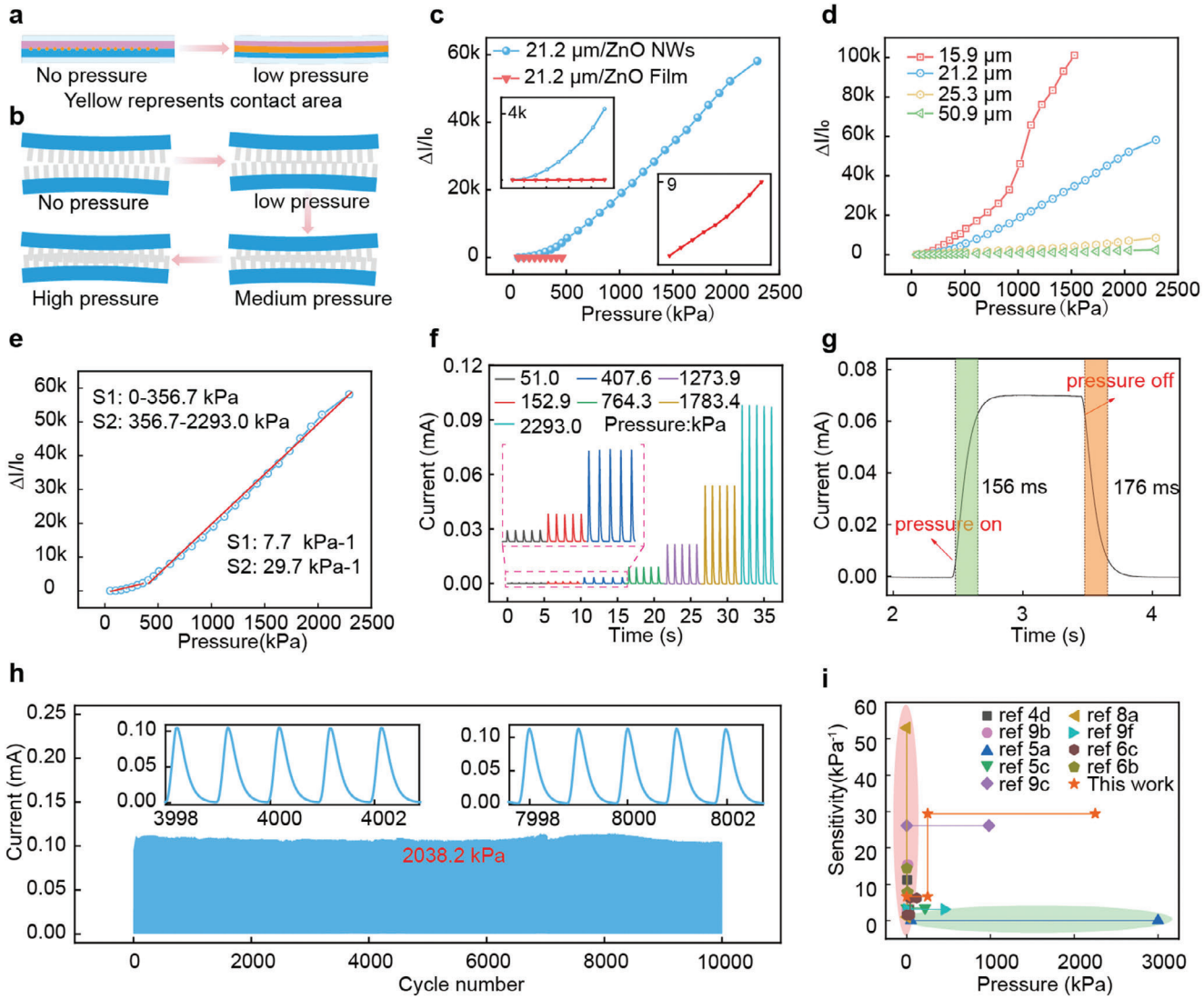

Figure 3. Sensing Principle and Performance Evaluation of TPU/ZnO NWs Flexible Piezoresistive Sensors with a 3D Interlocking Structure. a) Schematic representation of the contact in the ZnO film. b) Schematic depiction of the contact between ZnO NWs. c) Comparative performance analysis between TPU/ZnO thin film and TPU/ZnO NWs in the sensitive layer. d) Performance comparison of sensitive layers with four different thicknesses (TPU/ZnO). e) Sensitivity curve of the device with a spinning thickness of 21.2 μm. f) Dynamic response curve of the piezoresistive sensor. g) Response time and recovery time of the piezoresistive sensors. h) Stability test of the piezoresistive sensor undergoing 10 000 cycles at a pressure of 2038.2 kPa. i) Comparative performance chart between this study and other relevant studies.

planes of ZnO (100), (002), (101), (102), (110), and (103), respectively. These values are consistent with the positions of the crystal planes reported in the XRD diffraction peak of ZnO literature.[10b] Figure 2e presents a magnified electron microscope image of the sensitive layer, indicating the uniform and dense growth texture of ZnO nanowires, affirming the successful growth of ZnO nanowires. Furthermore, the morphology of the sensitive layer TPU/ZnO NWs after exposure to pressure is captured in Figure S2 (Supporting Information), demonstrating that the ZnO nanowires on the surface remain intact without fracturing or collapsing under high pressure. Finally, Figure 2f exhibits a cross-section of the sensitive layer of TPU/ZnO NWs, illustrating that the ZnO nanowires grow 360° around the spun filaments, ensuring good contact between neighboring nanowires both above and below. Due to the curvature of the cylindrical filament skeleton at the bottom, the zinc oxide nanowires form a loose top and a tight bottom within the spinning skeleton, providing a conducive condition for the interlocking structure capable of withstanding higher pressure without compromising film recovery post-pressure application.

Figure 3a,b depict the planar structure of the TPU/ZnO film and the sensing mechanism of TPU/ZnO NWs in the flexible resistive sensor. The planar spinning structure is generated by employing a spinning skeleton of TPU and magnetron sputtering of zinc oxide nanoparticles. Figure 3a illustrates the contact between TPU/ZnO thin films, with the upper and lower layers represented by pink and blue, respectively. Initially, there are fewer yellow contact points (contact area) between the films. Upon

applying slight pressure, the 2D skeleton deforms rapidly, saturating the contact area between the films, resulting in a minimal change in current with pressure, as indicated by the red test line in Figure 3c. The rapid saturation of the contact area leads to low sensitivity and a narrow linear testing range. In Figure 3b, the presence of ZnO NWs array around TPU causes increased spatial deformation of the thin film in the sensing layer. The transition from no pressure to low pressure induces changes in the spatial deformation of the film. Additionally, the support of nanowires leads to a reduction in initial resistance, resulting in higher sensitivity under low pressure compared to the planar structure. As pressure increases, zinc oxide nanowires interweave, expanding the contact area and reducing contact resistance. The movement of nanowires under pressure increases the resistance between them. Uniform pressure variation causes an even change in the contact area of ZnO NWs, ultimately leading to an exceptionally wide linear range in sensitivity curves.

We employed different spinning times to spin films with four different thicknesses, testing and comparing TPU/ZnO films and TPU/ZnO NWs structures with different thicknesses, as shown in Figure S4 (Supporting Information). The results indicate a significant improvement in sensitivity and detection range for the zinc oxide nanowire structure compared to the zinc oxide film structure. When the film thickness is substantial, the detection range is essentially the same for both, but there is still a considerable difference in sensitivity. In addition to exploring the impact of the ZnO material's structure on performance, we investigated the performance of sensitive layers with different thicknesses of TPU/ZnO NWs. The performance tests for four different sensitive layer thicknesses are shown in Figure 3d. The results indicate a correlation between the thickness of the film and its level of deformation under pressure. Thinner films exhibit greater deformation changes and higher sensitivity, albeit at the cost of a reduced detection range. Thicker films, on the other hand, show less deformation under the same pressure, resulting in a broader detection range but lower sensitivity. Therefore, after comprehensive consideration, we selected a thickness of 21.2 μm for further study.

The curve in Figure 3e demonstrates a sensitivity of 7.7 kPa^{-1} within the low-pressure range of 0–356.7 kPa, attributed to the deformation changes in the film and the lack of an interlocking structure. Conversely, within the high-pressure range of 356.7–2293.0 kPa, the sensitivity is 29.7 kPa^{-1} due to the interlocking structure in the rotating skeleton and the unique structure of nanowires, leading to an increase in the contact area with increasing pressure. To demonstrate the repeatability of the flexible pressure sensor, we tested the consistency of five different devices, as shown in Figure S5 (Supporting Information). The initial current values of the five devices are shown in Figure S5b (Supporting Information), indicating that the encapsulation process does not unduly affect its initial resistance. We also conducted tests on the *I–V* curves of the sensor, as presented in Figure S6 (Supporting Information), which exhibited favorable current-voltage characteristics. These I-V curves exhibit rectification characteristics due to the formation of Schottky contact between ZnO and Au electrodes. Figure 3f shows a stable real-time dynamic response within the pressure range of 51.0 to 2293.0 kPa, as demonstrated in Figure S7 (Supporting Information), featuring more pressure dynamic responses. Minimum pressure detection for the device was tested and explained in Figure S8 (Supporting Information). Consistent step responses were observed by adding small acrylic acid segments. The response time and recovery time of the sensor were 156 and 176 ms, respectively, as depicted in Figure 3g.

To assess the stability of the sensor, experiments were conducted to evaluate its response to step pressure under mechanical conditions. Figure S9 (Supporting Information) illustrates the results. The current bias rates at the loading and unloading ends ranged from 2–7%, indicating excellent stability of our device under mechanical step pressure. As shown in Figure 3h, the stability of the sensor was also tested through 10 000 cycles of loading/unloading at an extremely high pressure of 2038.2 kPa. The curves in the graph show no significant fluctuations, demonstrating that the sensor maintains high stability even under extremely high pressure.

Currently, research on flexible pressure sensors spans a wide range, with most studies focusing on achieving high sensitivity while neglecting larger detection ranges, as indicated by the red portion in Figure 3i. In contrast, as shown in the green portion of Figure 3i, some work has achieved wider detection ranges but with extremely low sensitivity. Our research provides a solution to the challenge of balancing sensitivity and a wide detection range, proving its significant superiority over other current flexible pressure sensors.

Our TPU/ZnO NWs flexible pressure sensor exhibits high sensitivity and a broad linear detection range, making it a versatile wearable device for physiological and motion signal monitoring. As shown in **Figure** 4a, when the TPU/ZnO NWs pressure sensor is attached to the wrist, it demonstrates the ability to detect faint pulse signals. The data plot of the detected signals reveals three characteristic peaks of the pulse wave, labeled as P (pressure wave), T (tidal wave), and D (relaxation wave), located in the lower right corner. Figure 4b,c evaluate signal variations induced by wrist and elbow bending movements. The pressure applied to the joint sensor and its corresponding signal continuously increases with the increment of the bending angle. Abrupt large-angle bending of the wrist or elbow may lead to injuries. Monitoring pressure signals can prevent excessive bending of the wrist and elbow, thereby preventing potential harm. Finger bending is of significant importance in medical monitoring, commonly used in clinical practice to monitor the rehabilitation progress of individuals in a vegetative state. As shown in Figure 4d, it displays pressure signals under different degrees of finger bending. Notably, such signals can be applied to various applications, including prosthetics, bio-robots, and rehabilitation devices. Figure 4e,f demonstrate significant pressure signals generated during walking by the toes and heels, which can be utilized to correct and improve improper posture during walking through changes in pressure signals. Finally, Figure 4g tests the sole pressure signal when jumping to the ground, showcasing the excellent performance of the sensor under high pressure. The same sensor, as a wearable device, accurately measures both small physiological pressure signals and large motion pressure signals, highlighting the enormous potential application of the TPU/ZnO NWs pressure sensor in a wide range of wearable devices.

Furthermore, we demonstrate the fabrication of a sensor array with this wide linear detection range. Utilizing PDMS as a flexible substrate for the large-area sensor array, we manufactured

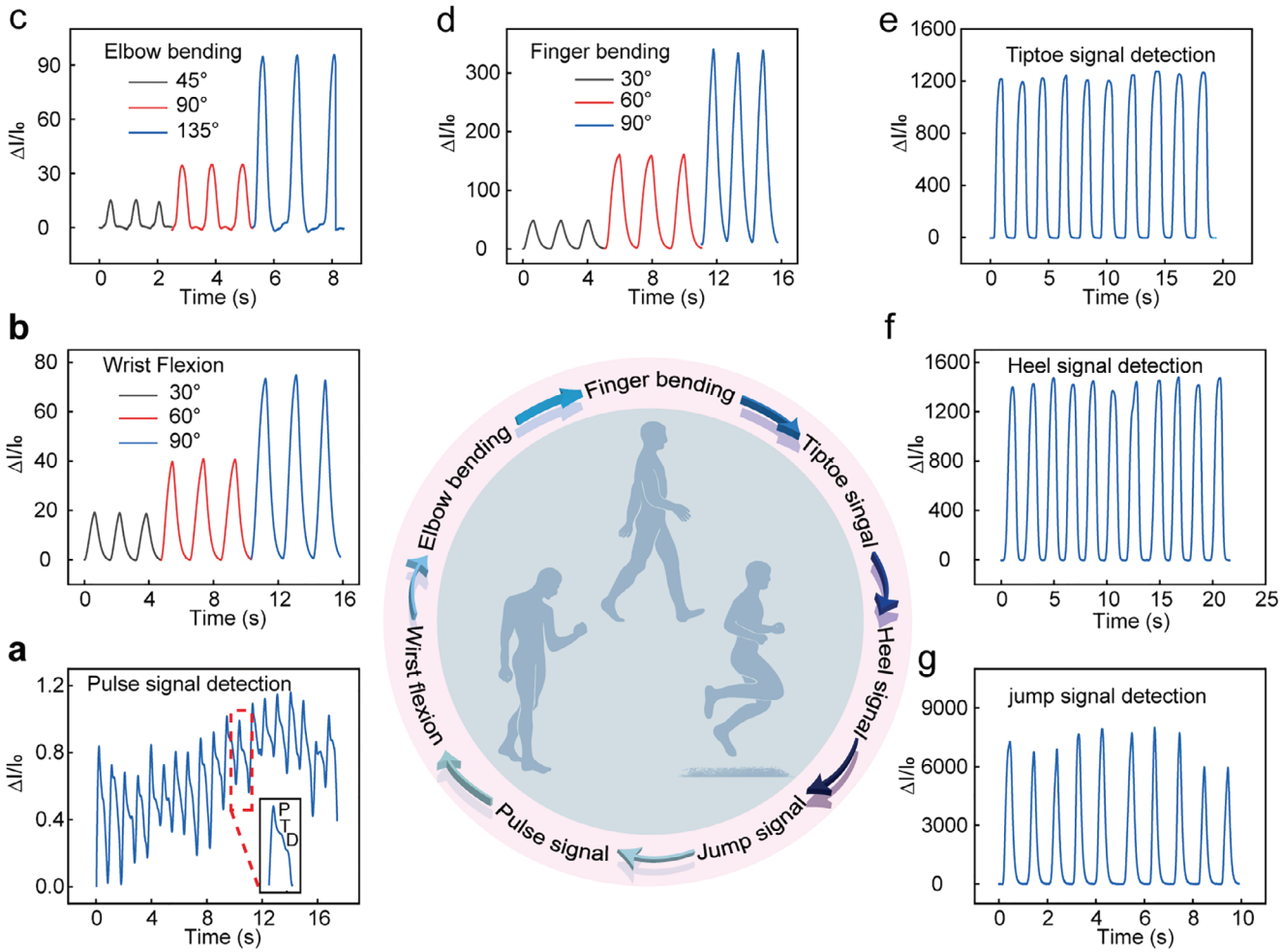

Figure 4. Utilization of a 3D Interlocking Structure-Based Flexible Piezoresistive Sensor for TPU/ZnO NWs in Human Motion Signal Monitoring. a) Monitoring of Weak Radial Artery Pulse: Local magnification displays three characteristic peaks of a typical pulse wave – P (percussion wave), T (tidal wave), and D (diastolic wave). b) Angular Response of Wrist Joint: Detection of wrist joint motions at angular positions of 30°, 60°, and 90°. c) Angular Response of Elbow Joint: Detection of elbow joint motions at angular positions of 45°, 90°, and 135°. d) Finger Bending: Detection of finger bending motions at angular positions of 30°, 60°, and 90°. e) Pressure Response from Tiptoe during Walking. f) Pressure Response from Heel during Walking. g) Pressure Signal Generated during Jumping.

gold electrodes through magnetron sputtering, as depicted in Figure S10 (Supporting Information). Laser engraving was employed to mark the gold electrodes after magnetron sputtering, followed by laser ablation to eliminate any excess gold in the corresponding areas. The electrode design is illustrated in the upper right corner of **Figure** 5a, with electrode photos shown in Figure S11 (Supporting Information). In Figure 5b, the marked upper and lower intersecting square electrodes are aligned with the sensitive TPU/ZnO NW layer. Finally, wires are led out from the electrodes, resulting in the preparation of a flexible sensor array. The flexible pressure resistive sensor array in this study can detect pressure distribution, as demonstrated in Figure 5c. To test the sensor array, a 50 g weight was placed at the center of the array, as shown in the optical schematic above Figure 5c. The pressure distribution results reveal distinct pressure responses in all four small regions at the center. Additionally, pressure mapping tests were conducted by pressing the index finger and thumb onto the array, as shown in Figure 5d,e. According to the schematic and pressure response diagrams, it is evident that when the index finger is pressed in the middle four sections, the top right corner exhibits the most prominent pressure response. This infers that the array can identify the region where an individual habitually applies force when pressing with the index finger. When the thumb is pressed, the response to pressure is apparent in the two areas on the right side. This indicates that the array can recognize the regions where an individual habitually applies force when pressing with the thumb. Figure S12 (Supporting Information) shows the change in cracks and resistance after applying pressure 100 times. The resistance change is negligible compared to the working resistance range (5 kΩ–50 MΩ) of the sensitive layer, indicating the stability of the device. This flexible tactile sensor utilizing resistive pressure technology has the capability to detect force patterns of individual fingers during pressing and can differentiate individuals based on force habits. This suggests considerable potential for the sensor in future intelligent recognition applications.

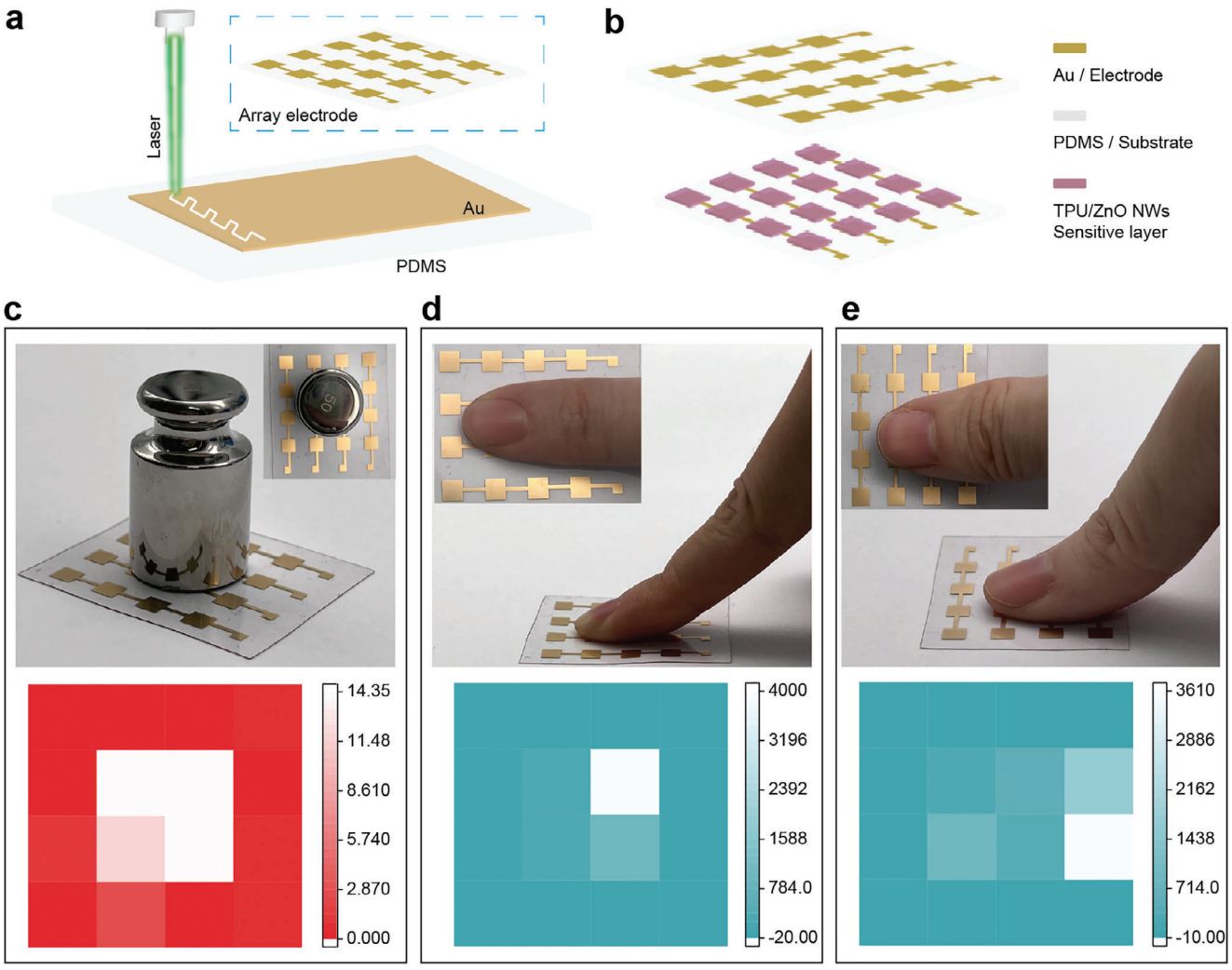

Figure 5. Fabrication and Evaluation of a TPU/ZnO NWs Flexible Piezoresistive Sensor Array with a 3D Interlocking Structure. a) Illustrative diagram of laser marking with gold electrodes. b) Schematic diagram of a fully crossed sensor array. c) Schematic diagram of pressure response on the array when weights are applied in a 4 × 4 pattern. d) Schematic diagram of pressure response on the array when the index finger is pressed in a 4 × 4 pattern. e) Schematic diagram of pressure response on the array when the thumb is pressed in a 4 × 4 pattern.

3. Conclusion

This paper reports on a flexible pressure sensor based on a 3D interlocking structure using TPU/ZnO NWs. Initially, a multi-layered film with interwoven fibers was prepared using electrospinning, and ZnO nanowire arrays were uniformly grown on the fiber surfaces through a hydrothermal method. The zinc oxide nanowire array formed a 3D interlocking structure between TPU fibers, effectively increasing the contact area and compressibility. By adjusting the thickness of the TPU fiber film and the structure of the zinc oxide nanowires, a flexible pressure sensor with high sensitivity (29.7 kPa^{-1}) and an ultra-wide linear detection range (356.7 to 2250 kPa) was achieved. The pressure signal exhibited excellent stability when tested 10 000 times under high pressure at 2038.2 kPa. When integrated into a wearable device, this device demonstrated a robust pressure response to both weak physiological pressure signals and strong motion-induced pressure signals. Its high sensitivity and linearity in both low and high pressure ranges ensure the majority of physiological and motion signal monitoring in daily life. Furthermore, the array integration enabled the identification of the applied position and pressure level of weights, along with the analysis of the primary force points on the fingers during pressing. These remarkable features indicate significant potential applications of the sensor in wearable electronics, human-machine interfaces, and health monitoring.

4. Experimental Section

Materials: Zinc oxide target material and gold target material (ZnO, 99.99%, Au, 99.999%). The target materials were procured from Zhongnuo Advanced Materials (Beijing) Technology Co., Ltd. Other materials used include N-N-Dimethylformamide (DMF, C_3H_7NO, MW = 73.09) from Aladdin Reagents (Shanghai) Co., Ltd., Tetrahydrofuran (THF, C_4H_8O, MW = 72.107) from Aladdin Reagents (Shanghai) Co., Ltd., Zinc nitrate hexahydrate ($H_{12}N_2O_{12}Zn$, MW = 297.49), Methenamine

($C_6H_{12}N_4$, MW = 140.19), Thermoplastic Urethane (TPU, MW = 90 000), and Electrode materials including Printed Circuit Board flexible electrode sheets, Polydimethylsiloxane (PDMS film, Thickness = 200 µm), Polyethylene terephthalate (PET Film, Thickness = 200 µm), Kapton double-sided tape, Poly tetra fluoroethylene (PTFE film, Thickness = 80 µm), and Conductive copper wire.

Manufacturing of the Sensitive Layer Nanofiber thin Films and Complete Devices: Initially, 2.82 g of TPU particles were accurately weighed and placed in a bottle, and subsequently, a mixture of 8 mL each of N-N-Dimethylformamide (DMF) and tetrahydrofuran was added to the bottle. The resulting mixture underwent stirring for 4 h at 70 °C using a heating and stirring station. Subsequently, the solution was transferred into a 5 mL syringe, and prepared for electrostatic spinning. A release paper was adhered to the drum collector, and parameters were set at a positive voltage of 14 kV, a negative voltage of −0.1 kV, a jet speed of 1 mL/h, and a drum speed of 260 rpm. After determining the spinning time, the process was completed. Finally, paste Kapton double-sided tape on one side of the square PET (Polyethylene terephthalate) frame, paste it on the spun film after electrospinning, and cut it along the edge of the PET frame to obtain the patterned spinning TPU film.

Following this, the PET backframe was securely fixed onto the substrate tray of the magnetron sputtering system and placed into the instrument. A high vacuum was established, raising the molecular pump to 100%, and the magnetron sputterer achieved a high vacuum of 5×10^{-5} Pa. The molecular pump was then adjusted to 50%, the glow power was set to 50 W, and the airflow was maintained at 100 sccm. Finally, the coating power was adjusted to 60 W, the airflow to 28 sccm, and the magnetron sputtering for the ZnO seed layer was performed for a duration of 25 min. The process was repeated for the other side of the film, and the ZnO seed layer was successfully prepared after plating on both sides.

After the preparation of the electrostatic spinning seed layer, the film was affixed to the substrate (with a significant gap at the bottom) and positioned facing downward inside a sealed container. Subsequently, a growth solution for ZnO nanowire development was introduced. A solution comprising 70 mL of hexamethylenetetramine and zinc nitrate hexahydrate at a concentration of 200 mmol L^{-1} was mixed with 260 mL of water to form a 400 mL growth solution. The mixture underwent ultrasonication for 10 min to ensure thorough mixing. The container was then placed in an oven set at 85 °C for 4 h, followed by removal, rinsing, and drying at 40 °C. ZnO nanowires were similarly grown on the other side. Following growth and drying, two PCB flexible gold electrodes were affixed to the PTFE tape, and a sensitive layer was then placed on the gold-plated surface of one electrode. The PTFE tape was folded to align the two circular electrodes, and the final step involved pre-pressure to complete the fabrication of a resistive sensor.

Characterization and testing of materials included scanning electron microscopy (Nova NanoSEM 450) to observe the surface morphology of TPU/ZnO NWs thin films of various sizes and device cross-sections. X-ray diffraction (XRD) analysis (Xpert3 powder) was employed for phase analysis of the TPU/ZnO NWs films. The resistance signal parameters of the device were tested using a DS345 function generator, SR570 current amplifier, LCR meter (E4980A), tensile testing machine (YL-S71), load sensors (SAS-5KG & HZC-T-10KG), and linear motor (R-LP3). Sample preparation utilized a heated magnetic stirrer (MS7-H550-PRO), oven (DKN312C), ultrasonic cleaning machine (KQ-800KDE), and balance (Mettler PL-402).

Supporting Information

Supporting Information is available from the Wiley Online Library or from the author.

Acknowledgements

J.H and S.W. contributed equally to this work. The authors thank the support of the National Natural Science Foundation of China (No. 52192610, 62422120), the Natural Science Foundation of Beijing (L223006), the National Key R&D Program of China (2021YFB3200302 and 2021YFB3200304), the Shenzhen Science and Technology Program (KQTD20170810105439418) and the Fundamental Research Funds for the Central Universities for their support.

Conflict of Interest

The authors declare no conflict of interest.

Data Availability Statement

The data that support the findings of this study are available from the corresponding author upon reasonable request.

Keywords

flexible electronics, interlocking structure, micro-structure, pressure sensors, wide range sensors

Received: October 6, 2024
Revised: November 11, 2024
Published online:

[1] a) Y. Liu, J. Tao, Y. Mo, R. Bao, C. Pan, *Adv. Mater.* **2024**, *36*, 2313857; b) S. Pyo, J. Lee, K. Bae, S. Sim, J. Kim, *Adv. Mater.* **2021**, *33*, 2005902; c) X. Wang, L. Dong, H. Zhang, R. Yu, C. Pan, Z. L. Wang, *Adv. Sci.* **2015**, *2*, 1500169; d) W. Gao, J. Huang, J. He, R. Zhou, Z. Li, Z. Chen, Y. Zhang, C. Pan, *InfoMat.* **2023**, *5*, e12426; e) Q. Hua, J. Sun, H. Liu, R. Bao, R. Yu, J. Zhai, C. Pan, Z. L. Wang, *Nat. Commun.* **2018**, *9*, 244; f) R. Bao, J. Tao, J. Zhao, M. Dong, J. Li, C. Pan, *Sci. Bull.* **2023**, *68*, 1027; g) B. Shih, D. Shah, J. Li, T. G. Thuruthel, Y. L. Park, F. Iida, Z. Bao, R. Kramer-Bottiglio, M. T. Tolley, *Sci. Robot.* **2020**, *5*, eaaz9239; h) X. Liu, *Science.* **2020**, *370*, 910.

[2] a) R. Chen, T. Luo, J. Wang, R. Wang, C. Zhang, Y. Xie, L. Qin, H. Yao, W. Zhou, *Nat. Commun.* **2023**, *14*, 6641; b) J. Tao, M. Dong, L. Li, C. Wang, J. Li, Y. Liu, R. Bao, C. Pan, *Microsyst. Nanoeng.* **2020**, *6*, 62; c) Y. Liu, R. Bao, J. Tao, J. Li, M. Dong, C. Pan, *Sci. Bull.* **2020**, *65*, 70; d) B. Ji, Q. Zhou, B. Hu, J. Zhong, J. Zhou, B. Zhou, *Adv. Mater.* **2021**, *33*, 2100859.

[3] a) L. Zhang, Y. P. Mo, W. D. Ma, R. Wang, Y. X. Wan, R. R. Bao, C. F. Pan, *ACS Appl. Elect. Mater.* **2023**, *5*, 5823; b) X. Li, Y. J. Fan, H. Y. Li, J. W. Cao, Y. C. Xiao, Y. Wang, F. Liang, H. L. Wang, Y. Jiang, Z. L. Wang, G. Zhu, *ACS Nano.* **2020**, *14*, 9605; c) K. K. Zhou, Y. Zhao, X. P. Sun, Z. Q. Yuan, G. Q. Zheng, K. Dai, L. W. Mi, C. F. Pan, C. T. Liu, C. Y. Shen, *Nano Energy.* **2020**, *76*, 105035; d) J. Jia, Y. Zhu, P. Das, J. Ma, S. Wang, G. Zhu, Z.-S. Wu, *J. Materiomics.* **2023**, *9*, 1242; e) R. Shi, T. Lei, Z. Xia, M. Wong, *J. Semicond.* **2023**, *44*, 091601; f) Y. Shi, Z. Zhang, Q. Huang, Y. Lin, Z. Zheng, *J. Semicond.* **2023**, *44*, 5504; g) R. Yin, L. Li, L. Wang, Z. Lou, *J. Semicond.* **2023**, *44*, 032602; h) J. Park, M. Kim, Y. Lee, H. S. Lee, H. Ko, *Sci. Adv.* **2015**, *1*, 1500661.

[4] a) K. H. Ha, W. Zhang, H. Jang, S. Kang, L. Wang, P. Tan, H. Hwang, N. Lu, *Adv. Mater.* **2021**, *33*, 2103320; b) H. Xu, L. Gao, Y. Wang, K. Cao, X. Hu, L. Wang, M. Mu, M. Liu, H. Zhang, W. Wang, Y. Lu, *Nanomicro Lett.* **2020**, *12*, 159; c) Q. Wu, Y. Qiao, R. Guo, S. Naveed, T. Hirtz, X. Li, Y. Fu, Y. Wei, G. Deng, Y. Yang, X. Wu, T. L. Ren, *ACS Nano.* **2020**, *14*, 10104; d) Y. K. Pang, X. C. Xu, S. E. Chen, Y. H. Fang, X. D. Shi, Y. M. Deng, Z. L. Wang, C. Y. Cao, *Nano Energy.* **2022**, *96*, 107137.

[5] a) Y. Jeong, J. Gu, J. Byun, J. Ahn, J. Byun, K. Kim, J. Park, J. Ko, J. H. Jeong, M. Amjadi, I. Park, *Adv. Healthcare Mater.* **2021**, *10*, 2001461; b) Y. Zhang, J. Yang, X. Hou, G. Li, L. Wang, N. Bai, M. Cai, L. Zhao, Y.

Wang, J. Zhang, K. Chen, X. Wu, C. Yang, Y. Dai, Z. Zhang, C. F. Guo, *Nat. Commun.* **2022**, *13*, 1317; c) T. Zhao, L. Yuan, T. Li, L. Chen, X. Li, J. Zhang, *ACS Appl. Mater. Interfaces.* **2020**, *12*, 55362; d) D. Geng, S. Chen, R. Chen, Y. You, C. Xiao, C. Bai, T. Luo, W. Zhou, *Adv. Mater. Tech.* **2021**, *7*, 2101031.

[6] a) Z. Yu, J. Xu, H. Gong, Y. Li, L. Li, Q. Wei, D. Tang, *ACS Appl. Mater. Interfaces.* **2022**, *14*, 5101; b) M. Liu, X. Pu, C. Jiang, T. Liu, X. Huang, L. Chen, C. Du, J. Sun, W. Hu, Z. L. Wang, *Adv. Mater.* **2017**, *29*, 1703700; c) X. H. Cui, J. W. Chen, W. Wu, Y. Liu, H. D. Li, Z. G. Xu, Y. T. Zhu, *Nano Energy.* **2022**, *95*, 107022.

[7] a) C. L. Choong, M. B. Shim, B. S. Lee, S. Jeon, D. S. Ko, T. H. Kang, J. Bae, S. H. Lee, K. E. Byun, J. Im, Y. J. Jeong, C. E. Park, J. J. Park, U. I. Chung, *Adv. Mater.* **2014**, *26*, 3451; b) Z. Wang, S. Guo, H. Li, B. Wang, Y. Sun, Z. Xu, X. Chen, K. Wu, X. Zhang, F. Xing, L. Li, W. Hu, *Adv. Mater.* **2019**, *31*, 1805630; c) G. Schwartz, B. C. Tee, J. Mei, A. L. Appleton, D. H. Kim, H. Wang, Z. Bao, *Nat. Commun.* **2013**, *4*, 1859; d) B. Yin, X. Liu, H. Gao, T. Fu, J. Yao, *Nat. Commun.* **2018**, *9*, 5161; e) Y. Lu, X. Qu, W. Zhao, Y. Ren, W. Si, W. Wang, Q. Wang, W. Huang, X. Dong, *Research.* **2020**, *2020*, 2038560.

[8] a) T. Yang, W. Deng, X. Chu, X. Wang, Y. Hu, X. Fan, J. Song, Y. Gao, B. Zhang, G. Tian, D. Xiong, S. Zhong, L. Tang, Y. Hu, W. Yang, *ACS Nano.* **2021**, *15*, 11555; b) Y. Liu, H. Xu, M. Dong, R. Han, J. Tao, R. Bao, C. Pan, *Adv. Mater. Tech.* **2022**, *7*, 2200504; c) Z. Zhou, L. Wei, Y. Yi, S. Feng, Z. Zhan, D. Tian, C. Lu, *J. Materiomics.* **2023**, *9*, 1151; d) Y. Liu, J. Tao, W. Yang, Y. Zhang, J. Li, H. Xie, R. Bao, W. Gao, C. Pan, *Small.* **2022**, *18*, 2106906.

[9] a) Y. Lu, Y. He, J. Qiao, X. Niu, X. Li, H. Liu, L. Liu, *ACS Appl. Mater. Interfaces.* **2020**, *12*, 55169; b) S. Chun, I. Y. Choi, W. Son, G. Y. Bae, E. J. Lee, H. Kwon, J. Jung, H. S. Kim, J. K. Kim, W. Park, *Adv. Funct. Mater.* **2018**, *28*, 1804132; c) S. Pyo, J. Lee, W. Kim, E. Jo, J. Kim, *Adv. Funct. Mater.* **2019**, *29*, 1902484; d) X. Li, Y. Lin, L. Cui, C. Li, Z. Yang, S. Zhao, T. Hao, G. Wang, J. Y. Heo, J. C. Yu, Y. W. Chang, J. Zhu, *ACS Appl. Mater. Interfaces.* **2023**, *15*, 56233; e) S. Zhao, W. Ran, L. Wang, G. Shen, *J. Semicond.* **2022**, *43*, 082601; f) T. Yang, H. Pan, G. Tian, B. B. Zhang, D. Xiong, Y. Y. Gao, C. Yan, X. Chu, N. J. Chen, S. Zhong, L. Zhang, W. L. Deng, W. Q. Yang, *Nano Energy.* **2020**, *72*, 4270; g) C. Pang, G. Y. Lee, T. I. Kim, S. M. Kim, H. N. Kim, S. H. Ahn, K. Y. Suh, *Nat. Mater.* **2012**, *11*, 795; h) L. Pu, R. Saraf, V. Maheshwari, *Scientific Rep.* **2017**, *7*, 5834; i) M. S. Suen, Y. C. Lin, R. S. Chen, *Sensor. Actuat. A-phys.* **2018**, *269*, 574.

[10] a) D. Yuan, M. Chen, Y. Xu, L. Huang, J. Ma, Q. Peng, X. Cai, *J. Appl. Polym. Sci.* **2019**, *137*, 48469; b) M. Ahmad, C. F. Pan, J. Iqbal, L. Gan, J. Zhu, *Chem. Phys. Lett.* **2009**, *480*, 105.